Toroidal, compression, and vortical dipole strengths in $^{144-154}$Sm: Skyrme-RPA exploration of deformation effect

J. Kvasil[1], V.O. Nesterenko[2], W. Kleinig[2,3], D. Bozik[1], P.-G. Reinhard[4], and N. Lo Iudice[5,6],
[1] *Institute of Particle and Nuclear Physics, Charles University, CZ-18000, Praha 8, Czech Republic**
[2] *Laboratory of Theoretical Physics, Joint Institute for Nuclear Research, Dubna, Moscow region, 141980, Russia†*
[3] *Technische Universität Dresden, Inst. für Analysis,D-01062, Dresden, Germany*
[4] *Institut für Theoretische Physik II, Universität Erlangen, D-91058, Erlangen, Germany*
[5] *Dipartimento di Scienze Fisiche, Universitȧ di Napoli Federico II, Monte S Angelo, Via Cintia I-80126 Napoli, Italy and*
[6] *Istituto Nazionale di Fisica Nucleare, Sezione di Napoli, Monte S Angelo, Monte S Angelo, Via Cintia I-80126 Napoli, Italy*

(Dated: April 26, 2021)

A comparative analysis of toroidal, compressional and vortical dipole strengths in the spherical ^{144}Sm and the deformed ^{154}Sm is performed within the random-phase-approximation using a set of different Skyrme forces. Isoscalar (T=0), isovector (T=1), and electromagnetic excitation channels are considered. The role of the nuclear convection $j_{\rm con}$ and magnetization $j_{\rm mag}$ currents is inspected. It is shown that the deformation leads to an appreciable redistribution of the strengths and causes a spectacular deformation splitting (exceeding 5 MeV) of the isoscalar compressional mode. In ^{154}Sm, the μ=0 and μ=1 branches of the mode form well separated resonances. When stepping from ^{144}Sm to ^{154}Sm, we observe an increase of the toroidal, compression and vortical contributions in the low-energy region (often called pygmy resonance). The strength in this region seems to be an overlap of various excitation modes. The energy centroids of the strengths depend significantly on the isoscalar effective mass m_0. Skyrme forces with a large m_0 (typically $m_0/m \approx 0.8-1$) seem to be more suitable for description of experimental data for the isoscalar giant dipole resonance.

PACS numbers: 24.30.Cz,21.60.Jz,13.40.-f,27.80.+w

I. INTRODUCTION

Possible evidence of a vortical flow in nuclei was suggested by the analysis of the structure of the isoscalar giant dipole resonance (ISGDR) observed in (α,α') scattering experiments [1–5] (see Ref. [6] for a review and an exhaustive list of references). In fact, the prevailing conclusion from this analysis was that the high-energy peak of the ISGDR is produced by compressional vibrations [7, 8], whereas the low-energy bump should be attributed to vortical nuclear flow associated with a toroidal dipole mode [9–12]. The toroidal moments emerge as second order terms of multipole expansions of electric currents in physical systems [13, 14]. In nuclei, the toroidal mode (TM) was predicted within a hydrodynamical model [15].

On the other hand, it was argued that a strong mixing between compressional and vortical vibrations in the isoscalar E1 states should be expected [12]. Moreover, it is not yet completely settled how the vorticity relates to the toroidal and compressional modes. This depends on the way the vorticity is defined. In hydrodynamical (HD) models, where it is characterized by a non-vanishing curl of the velocity field [16], the vorticity is solely associated to the TM while the compressional mode (CM) is irrotational. An alternative definition, more linked to nuclear observables, was proposed by Ravenhall and Wambach (RW) [17]. It adopts, as a measure of the vorticity, the multipole component $j^{(fi)}_{\lambda l=\lambda+1}(r)$ of the transition density current $\langle f|\hat{\vec{j}}_{\rm nuc}(\vec{r})|i\rangle$. The motivation for this choice is that this component is not constrained by the continuity equation. With this measure of the vorticity, the TM and CM describe mixed flows of both vortical and irrotational nature. In the recent study [18], the vortical operator of RW type was derived and related in a simple manner to the CM and TM operators. Then the vortical, toroidal and compression E1 strengths in ^{208}Pb were compared and thoroughly scrutinized within a separable random-phase-approximation (SRPA) [19, 20] using the SLy6 Skyrme force [21]. Later a similar study was performed for the isotopes ^{100,124,132}Sn [22].

Following the above SRPA exploration, the TM falls into the energy region of so-called pygmy dipole resonance (PDR) [6] supposed to be induced in neutron rich nuclei by a relative translational oscillation of the neutron skin against the residual N=Z core. So an interplay of TM and PDR may be expected. As shown in our recent study [23] within the full (non-separable) RPA [24], the PDR energy region indeed embraces various modes with a strong TM fraction. Moreover, the vortical flow dominates in the nuclear interior while the irrotational motion (relevant for E1 transitions in the long-wave approximation) prevails at the nuclear surface. This point deserves a further investigation. In particular, a comparative analysis of experimental data from $(\alpha,\alpha'\gamma)$ (relevant for both TM and PDR in T=0 channel), (γ,γ') observations (e.g. in Sn isotopes [25] and N=82 isotones

*Electronic address: kvasil@ipnp.troja.mff.cuni.cz
†Electronic address: nester@theor.jinr.ru

[26]), and (e,e') reactions is needed.

In this study, we continue the exploration of the toroidal, compression and vortical (RW) E1 strengths in various mass regions using SRPA. While the previous analysis concerned ^{208}Pb [18] and Sn isotopes [22], the present study concentrates on Sm isotopes, from spherical ^{144}Sm to axially deformed ^{154}Sm. Thereby we look particularly at the influence of the nuclear deformation. Like in [22], we use a representative set of Skyrme forces (SLy6 [21], SkT6 [27], SVbas [28], SkM* [29], and SkI3 [30]) covering a wide range of the isoscalar effective mass, $m_0/m = 1-0.58$. The isoscalar (T=0), isovector (T=1), and pure proton (elm) channels of E1 excitations are considered. Like in [18, 22], the relative contributions to the strengths of the convection $j_{\rm con}$ and magnetization $j_{\rm mag}$ nuclear currents are inspected. To demonstrate the ability of our approach and accuracy of different Skyrme parametrizations, the supplemented characteristics (binding energies, photoabsorption cross sections, energy-weighted sum rules) are considered.

The SRPA method used in the present calculations has been already successfully applied to description of various kinds of nuclear excitations (electric [18, 31–34] and magnetic [35–37] giant resonances, E1 strength near the particle thresholds [34, 38], and TM/CM/RW modes [18, 22]) in both spherical and deformed nuclei and was shown as an efficient and reliable theoretical tool.

The paper is organized as follows. In Sec. II the theoretical background and calculation scheme are presented. In Sec. III, the supplemented characteristics are inspected and numerical results for TM, CM, and RW strengths are discussed. In Sec. IV, the conclusions are done. In Appendix A, the vortical, toroidal, and compression flows and their operators are discussed. The HD and RW conceptions of the vorticity on nuclear flow are outlined. Appendix B sketches the derivation of the RW equations. In Appendix C, a basic information about the SRPA method is given.

II. THEORETICAL BACKGROUND AND CALCULATION SCHEME

The main topic of this paper is the influence of nuclear deformation on the toroidal, compressional and vortical dipole strength functions. The corresponding transition operators are [18]

$$\hat{M}(\mathrm{tor};\,1\mu) = -\frac{2}{2\mathrm{c}\sqrt{3}}\int \mathrm{d^3r}\,\hat{\vec{\mathrm{j}}}_{\mathrm{nuc}}(\vec{\mathrm{r}}) \cdot\left[\frac{\sqrt{2}}{5}\,r^2\,\vec{Y}_{12\mu}(\hat{r}) + (r^2-\delta_{T,0}\langle r^2\rangle_0)\,\vec{Y}_{10\mu}(\hat{r})\right], \quad (1)$$

$$\hat{M}'(\mathrm{com};\,1\mu) = \frac{1}{10}\int \mathrm{d^3r}\,\hat{\rho}(\vec{\mathrm{r}}) \cdot\left[r^3-\delta_{T,0}\,\frac{5}{3}\,\langle r^2\rangle_0\,r\right] Y_{1\,\mu}(\hat{r}), \quad (2)$$

$$\hat{M}(\mathrm{vor};\,1\mu) = -\frac{\mathrm{i}}{5\mathrm{c}}\sqrt{\frac{3}{2}}\int \mathrm{d^3r\,r^2}\,\hat{\vec{\mathrm{j}}}_{\mathrm{nuc}}(\vec{\mathrm{r}})\cdot\vec{\mathrm{Y}}_{12\mu}(\hat{\mathrm{r}}), \quad (3)$$

where $\hat{\vec{j}}_{\rm nuc}(\vec{r})$ and $\hat{\rho}(\vec{r})$ are operator of nuclear current and nuclear density, respectively. Symbols $Y_{\lambda\mu}(\hat{r})$ and $\vec{Y}_{\lambda l\mu}(\vec{r})$ stand for spherical harmonics and vector spherical harmonics, respectively, and $\langle r^2\rangle_0 = \int d^3r\,\rho_0(\vec{r})\,r^2$ is the ground state square radius. The derivation of these operators and their connection to the long-wavelength limit of the standard E1 operator

$$\hat{M}(E\,1\mu) = -\int d^3r\,\hat{\rho}(\vec{r})\,r\,Y_{1\mu}(\hat{r}) \quad (4)$$

can be found in the Appendix A and Ref. [18]. The toroidal, compressional, and vortical strength functions

$$S'_{\gamma}(E1\,,\,E) = \sum_{\mu=0,\mp1}\sum_{\nu} |\,<\nu|\,\hat{M}(\gamma;\,1\mu)\,|0>\,|^2\,\xi_\Delta(E-E_\nu) \quad (5)$$

are calculated in the framework of the Skyrme SRPA approach [19, 20], see Appendix C for more detail. In the above expression, γ labels the TM ,CM, and RW strengths determined by the operators (1), (2), and (3), respectively. The indices ν stand for the RPA states with the energies E_ν, $|0>$ is the RPA ground state. Further,

$$\xi_\Delta(E-E_\nu) = \frac{1}{2\pi}\,\frac{\Delta}{(E-E_\nu)^2+(\frac{\Delta}{2})^2} \quad (6)$$

is the Lorentz weight with the averaging parameter Δ. The averaging is needed for the convenience of comparison of the results with the experimental data and to simulate roughly the smoothing effects beyond the SRPA (escape widths and coupling to complex configurations). For the broad and poorly known TM,CM, and RW strengths, a constant averaging width Δ=1 MeV is optimal. The strengths are analyzed in T=0, T=1, and electromagnetic (elm) channels characterized by the effective charges $e_q^{\rm eff}$ and gyromagnetic ratios $g_q^{\rm eff}$

$$T=0: \quad e_n^{\rm eff}=e_p^{\rm eff}=1,\; g_{n,p}^{\rm eff}=\frac{\zeta}{2}\,(g_n+g_p), \quad (7)$$

$$T=1: \quad e_n^{\rm eff}=-e_p^{\rm eff}=-1,\; g_{n,p}^{\rm eff}=\frac{\zeta}{2}\,(g_n-g_p), \quad (8)$$

$$elm: \quad e_n^{\rm eff}=0,\; e_p^{\rm eff}=1, \quad g_{n,p}^{\rm eff}=\zeta g_{n,p}\,, \quad (9)$$

where $g_n=-3.82$ and $g_p=5.58$ are free neutron and proton gyromagnetic ratios, $\zeta\approx0.7$ is the usual quenching factor [39]. See details in Appendix A.

The photoabsorption cross-section is fully determined by the $E1$ transitions and thus reads [40]

$$\sigma_{\rm phot}(E) = \frac{16\,\pi^3\,\alpha_e}{9\,e^2}\,E\,S(E1;\,E), \quad (10)$$

where $\alpha_e = 1/137$ is the fine-structure constant and $S(E1;\ E)$ is the strength function calculated with the standard dipole operator

$$\hat{M}(E1\mu) = \frac{N}{A}\sum_{p=1}^{Z} r_p Y_{1\mu}(\Omega_p) - \frac{Z}{A}\sum_{n=1}^{N} r_n Y_{1\mu}(\Omega_n)\ . \quad (11)$$

For the photoabsorption cross-section, detailed experimental data are available [41, 42]. So it is worth to compute this observable more accurately. It should be taken into account that i) the escape widths appear above the particle emission thresholds and grow with energy due to the widening of the emission phase space, ii) the collisional widths, induced by the coupling with complex configurations, also increase with the excitation energy. To simulate these trends, one should use in (6) an energy-dependent averaging parameter $\Delta(E)$. This can be done by implementing a double folding scheme [34]. We calculate first the strength function (5) with the operator (11) by using a small but fixed value of Δ. This gives the strength distribution $S'(E1;\ E)$ very closed to one obtained in RPA but with an equidistant energy grid. This strength is then folded again by using an energy dependent $\Delta(E)$:

$$S(E1;\ E) = \int dE'\ S'(E1;\ E')\ \xi_{\Delta(E')}(E - E'). \quad (12)$$

In the present study, we use a simple linear dependence

$$\Delta(E') = \begin{cases} \Delta_0 & \text{for } E' \le E_{\rm th} \\ \Delta_0 + a(E' - E_{\rm th}) & \text{for } E' > E_{\rm th} \end{cases} \quad (13)$$

where $E_{\rm th}$ is the energy of the first emission threshold and $\Delta_0 = 0.1$ MeV is a minimal width. The parameter a is chosen to reproduce the GDR strength distribution.

In order to test the sensitivity of the modes, we consider a selection of sufficiently different Skyrme parametrizations (SkT6 [27], SVbas [28], SkM* [29], SLy6 [21], and SkI3 [30]) covering a wide range of isoscalar effective masses: m_0/m=1, 0.9, 0.79, 0.69, and 0.58, respectively. All the parametrizations provide a good description of basic ground properties of nuclei.

The configuration space in the calculations covers all particle-hole (two-quasiparticle) states with an excitation energy up to $E_{\rm cut} \approx 175$ MeV. Such a big basis allows to exhaust in the SRPA calculations about 100% of the isovector Thomas-Reiche-Kuhn (TRK) energy-weighted sum rule (EWSR) [40] for the GDR and isoscalar Harakeh's EWSR for the ISGDR [43] (see also an extensive discussion at the end of the next subsection and Appendix C). Besides that, the large basis is crucial to lower the energy position of the spurious E1(T=0) peak towards the correct zero energy. In the present study, it lies in spherical ^{144}Sm at 1.5 – 2.0 MeV, depending on the Skyrme parametrization. This is not so good as in some full RPA calculations for ^{208}Pb, which use a larger configuration space and manage to yield the spurious peak below $\sim$ 0.6 MeV, see e.g. SLy5 [44] and SLy6 [23] results. However, the present value is sufficient for our aims since the T=0 strengths of interest are situated at $E > 5$ MeV and further extension of the configuration space does not significantly affect them. To be on the safe side, the TM, CM, and RW strength functions are given below only in the range $E > 5$ MeV.

The calculations exploit a 2D representation in cylindrical coordinates using a mesh size of 0.3 fm and a calculation box of 21 fm. For open-shell isotopes, we use zero-range pairing forces. The Hartree-Fock-Bogoliubov (HFB) equations are implemented at the BCS level [45]. For closed shell nuclei, this reduces automatically to a Hartree-Fock (HF) treatment.

III. RESULTS AND DISCUSSIONS

A. Supplemented characterisics

In Figures 1 and 2, some basic features (binding energies and photoabsorption cross sections) are presented to demonstrate the accuracy of our approach. In addition to spherical ^{144}Sm and deformed ^{154}Sm, the transitional isotopes ^{148,150,152}Sm are also shown to illustrate the trends with development of the deformation. The treatment of these soft isotopes within RPA is known to be insufficient and has to be amended by the coupling with complex configurations [46, 47]. Nevertheless, we find useful to present these RPA results to outline the trends.

In Figure 1, the binding energies of Sm isotopes

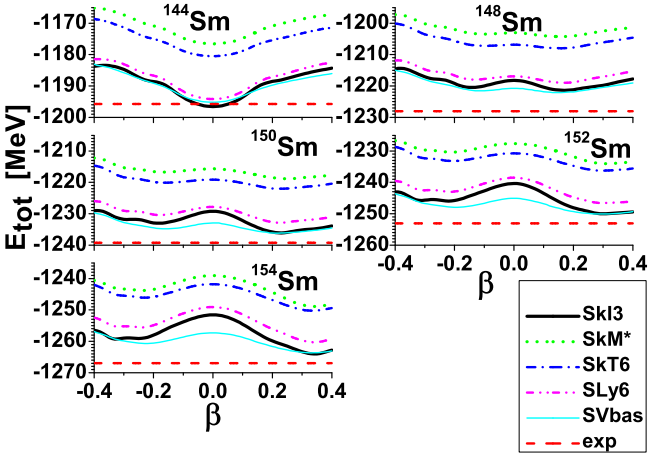

FIG. 1: (color online) HF/HFB binding energies of Sm isotopes versus the dimensionless parameter of quadrupole deformation β, calculated with different Skyrme parametrizations. The binding energies at an equilibrium deformation are to be compared with the experimental values (dashed horizontal lines) obtained from mass measurements [48]

.

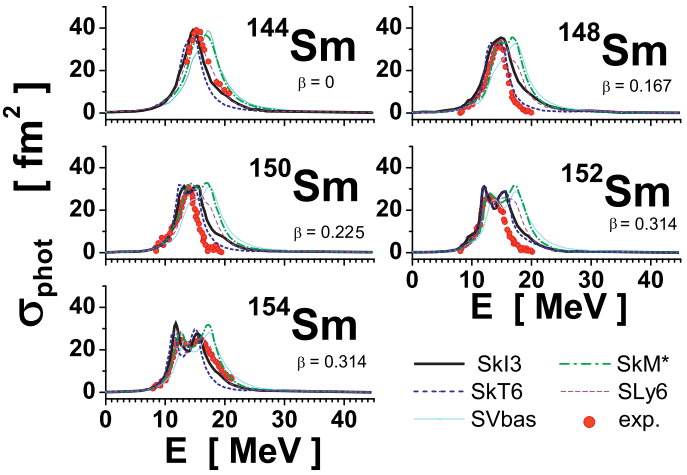

FIG. 2: (color online) Photoabsorption cross section versus excitation energy in $^{144-154}$Sm isotopes, calculated for different Skyrme parametrizations and compared with experimental values [42]. For each isotope, we indicate the dimensionless quadrupole deformation β of the prolate ground state computed with the force SLy6.

calculated within the HF/HFB approach are depicted in dependence on the dimensionless parameter of the quadrupole deformation β. For all Skyrme forces used here, we see the pronounced main minima at β=0 in the spherical ^{144}Sm and at β=0.33-0.34 in the prolate deformed ^{154}Sm. In the latter case, the internal quadrupole moment is Q=6.4-6.6 b. Both computed β and Q are in a good agreement with the experimental values $\beta_{\rm exp}$=0.34 and $Q_{\rm exp}$=6.6 b [66]. In the transitional ^{148,150,152}Sm, the calculations produce two shallow minima with roughly the same depth, corresponding to prolate and oblate shapes, respectively. Despite all the Skyrme parametrizations are fitted to experimental binding energies of selected doubly magic or semi-magic nuclei, in our calculations only the SLy6, SV-bas, and SkI3 forces reproduce the measured binding energy [48] in the semi-magic ^{144}Sm. The two older parametrizations SkM* and SkT6 were tuned to doubly-magic nuclei only and do not perform so well for the rather soft ^{144}Sm.

In Figure 2, the calculated photoabsorption cross section is inspected. We get a good agreement with experiment [42] for most Skyrme forces in the spherical ^{144}Sm and the well deformed ^{154}Sm. The deformation splitting of the GDR in ^{154}Sm is also reproduced. For the transitional isotopes, the agreement is acceptable as well. In all the nuclei, the main deviation arises at the high-energy wing of the GDR. This is probably an effect of neglecting the complex configurations.

Additional useful insight may be obtained from the analysis of the sum rules. As was mentioned above, the TRK sum rule for the photoabsorption cross section is exhausted in our calculations by about 100%, see details

TABLE I: The ISGDR (14) and RPA EWSR (in e^2 fm^{6}10^3 MeV) for CM(T=0) in ^{144,154}Sm, computed with different Skyrme forces.

		SkI3	SLy6	SkM*	SVbas	SkT6
^{144}Sm	ISGDR	24.4	24.7	25.1	24.3	24.4
	RPA	25.0	25.4	24.8	23.1	24.3
^{154}Sm	ISGDR	34.1	33.8	34.1	33.2	33.2
	RPA	34.8	34.0	33.5	32.6	33.1

in Appendix C. For the purposes of the present study, it is crucial to check the sum rule for the ISGDR [43]

$$\mathrm{EWSR}_{\mathrm{ISGDR}} = \frac{1}{100}\left[\frac{3\hbar^2}{8\pi m} A \left(11 \left\langle r^4 \right\rangle_0 - \frac{25}{3}\left\langle r^2 \right\rangle_0^2\right)\right], \quad (14)$$

obtained for the transition operator (2) and $\left\langle r^4 \right\rangle_0 = \int d^3r\, \rho_0(\vec{r})\, r^4$. The results are shown in Table I and they prove that this sum rule is also nicely fulfilled. Thus exhausting both isovector TRK and and isoscalar ISGDR E1 sum rules confirms that our configuration space is sufficiently large. Altogether, the above results demonstrate reliability of our approach in description of static and E1 dynamical properties of spherical and deformed nuclei and thus justifies its further application to TM/CM/RW E1 strength functions.

B. TM, CM, and RW strength functions

In Figure 3, the E1(T=0) and E1(T=1) strength functions for the CM in spherical ^{144}Sm and deformed ^{154}Sm are shown for the chosen set of Skyrme forces. The strengths are computed purely within the HF/HFB approach (without the residual interaction) by using the transition operator (2). As seen from the figure, the calculations give two broad CM bumps, a smaller one at low-energy and a large one at high-energy, which is in accordance to previous theoretical and experimental studies, see review [6]. In ^{154}Sm, the strength is larger and more uniform than in ^{144}Sm, as expected for a heavier and more deformed nucleus.

Three non-trivial effects are visible in both T=0 and T=1 channels. First, in ^{154}Sm we see a substantial growth of the CM strength in the region $4 \le E \le 11$ MeV where the PDR is supposed to appear. The comparison with the constrained case β=0 (no deformation) for the force SLy6 indicates that this effect should be mainly ascribed to increasing the number of neutrons (from magic 82 to 92). Indeed, unlike ^{144}Sm, in ^{154}Sm particular low-energy s.p. transitions $\nu\nu[1h_{9/2} \leftrightarrow 2f_{7/2}]$ become active, which may lead to the growth of the strength. However, following Fig. 4, where the deformation splitting of μ=0 and μ=1 CM(T=0) components for SkT6 and SLy6 forces is demonstrated, the deformation effect is also important. Just due to deformation, the low-energy

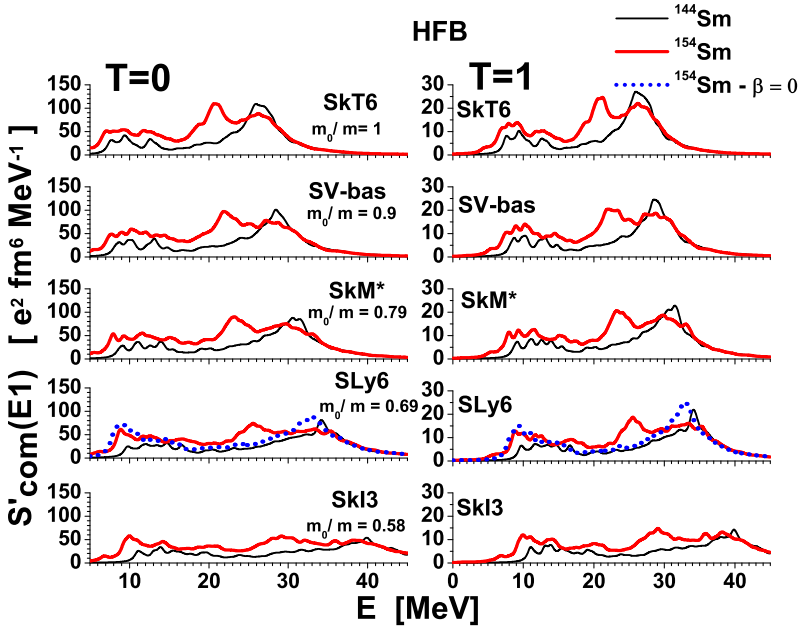

FIG. 3: (color online) Pure HF/HFB strength functions for T=0 (left) and T=1 (right) compression mode in spherical ^{144}Sm (black thin curve) and deformed ^{154}Sm (red bold curve) isotopes, computed with different Skyrme forces. For SLy6 in ^{154}Sm, we show also the strength computed for an artificial ground state forced to have β=0, i.e. stay spherical (blue dashed curve). On the left, the isoscalar effective masses m_0/m of the forces are listed.

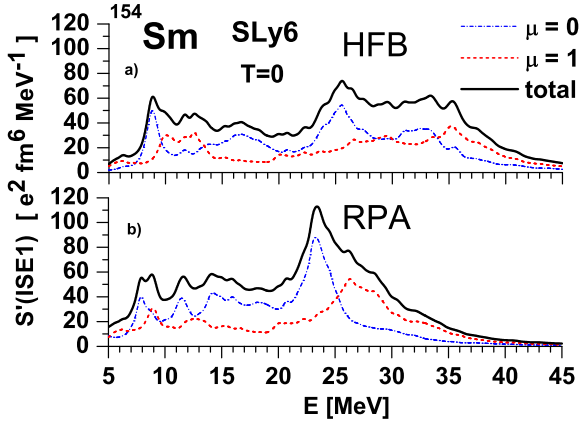

FIG. 4: (color online) Total (black bold), $\mu = 0$ (red dash), and $\mu = 1$ (blue dash-dotted) CM(T=0) strength functions in the deformed nucleus ^{154}Sm, computed with the force SLy6 within HFB (upper panel) and RPA (bottom panel) approaches.

and high-energy parts of the region $4 \leq E \leq 11$ MeV are dominated by μ=0 and μ=1 branches, respectively. Moreover, the comparison of T=0 and T=1 strengths allows to state that the PDR region may be also separated into two isospin sectors, a low-energy T=0 and a high-energy T=1 ones. This conjecture finds support in recent experimental analysis [25, 26], which have split the low-lying E1 spectra into an upper and lower energy sectors. The upper sector is excited solely in (γ, γ') and, therefore, has T=1 nature. The lower sector, instead, is composed of levels excited in both (γ, γ') and $(\alpha, \alpha'\gamma)$ and thus may be related to T=0 excitations.

Second, Fig. 3 shows that in ^{154}Sm a substantial bump appears at 20-30 MeV. This is particularly pronounced in T=0. The comparison to the case β=0 indicates that the bump is caused by the deformation. Fig. 4a) shows that this is just the μ=0 branch of the high-energy CM. We also see in Fig. 4a) a huge deformation splitting ($\sim$ 10 MeV) of the CM(T=0) strength computed with SLy6 force (similar results are obtained for other Skyrme forces). Thus deformation gives for the high-energy CM indeed dramatic effect.

Third, Fig. 3 shows that the CM strength in general and low-energy and high-energy CM bumps in particular are noticeably upshifted with decreasing m_0/m. This takes place for both isotopes ^{144}Sm and ^{154}Sm and in both channels, T=0 and T=1. The effect is straightforwardly explained by well known spread of s.p. spectra below the Fermi level with decreasing m_0/m, see examples in [49].

In Figure 5, the RPA CM strength functions are depicted. The residual interaction significantly downshifts (upshifts) the strength in T=0 (T=1) channels. Nevertheless all three effects discussed above for HF/HFB case remain the same. The (α, α') experiment [3, 5] gives for the ISGDR in ^{144}Sm two bumps with the energies and widths E=14.2 MeV, Γ=4.8 MeV and E=25.0 MeV, Γ=19.9 MeV. The narrow low-energy and broad high-energy bumps of the ISGDR are commonly treated as TM [10–12] and CM [7, 8], respectively. Alternatively,

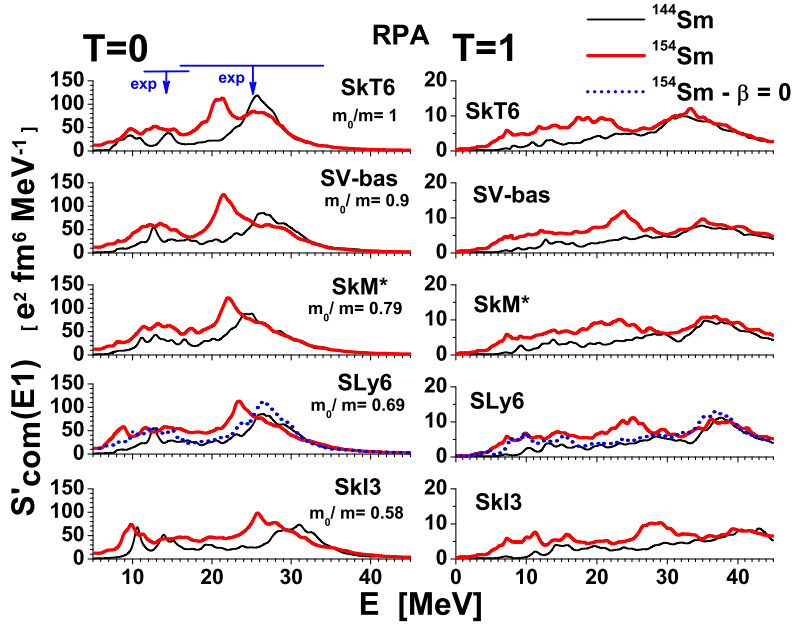

FIG. 5: (color online) The same as in Fig. 3 but for RPA compressional (CM) strength functions. The widths and energy centroids of the low- and high-energy ISGDR branches observed in (α, α') reaction [3, 5] are denoted at the upper/left panel.

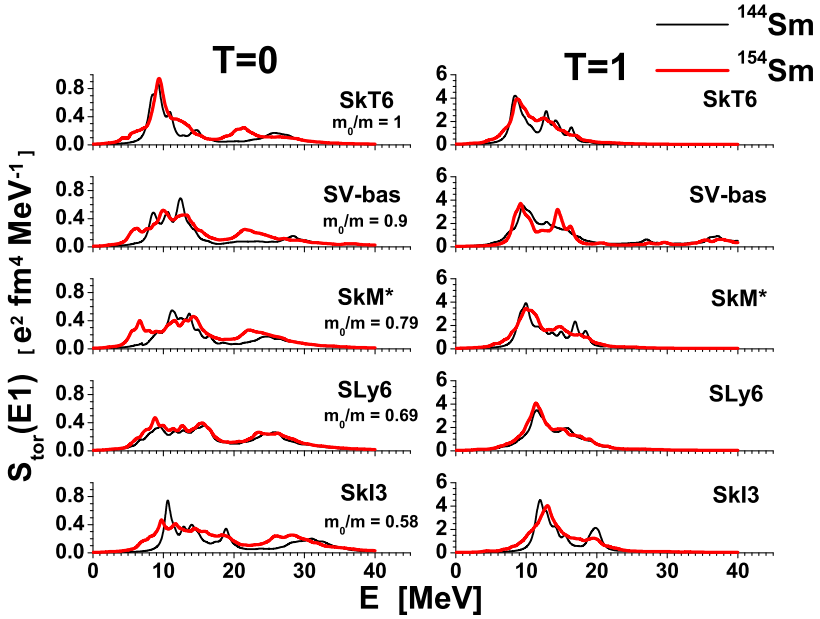

FIG. 6: (color online) The same as in Fig. 3 but for the RPA toroidal strength function.

both bumps may be treated as merely CM branches with the strong CM/TM coupling at a low energy [23]. Following Fig. 5, our calculations for ^{144}Sm roughly reproduce the experimental data [3, 5] for the forces SkT6, SVbas, SkM*, and SLy6. For SkI3 with a low effective mass m_0/m=0.58, the agreement for the high-energy CM bump is not so good. It seems that Skyrme forces with a large m_0/m are more preferable for description of CM.

Note that, following Fig. 4, the residual interaction considerably decreases the deformation splitting. As compared to the HFB case, it is reduced for the high-energy CM(T=0) bump from $\sim$ 10 MeV (HFB) to $\sim$ 5 MeV (RPA). Nevertheless, the deformation splitting remains very large. Such strong splitting is known only for the isovector GDR.

In Fig. 6, the RPA TM strength in ^{144,154}Sm is de-

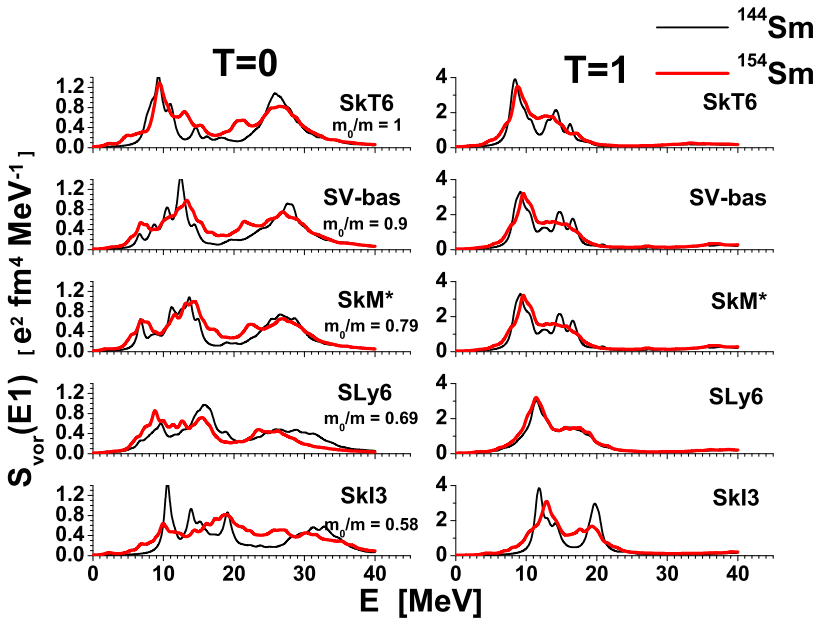

FIG. 7: (color online) The same as in Fig. 3 but for the RPA vortical (RW) strength function.

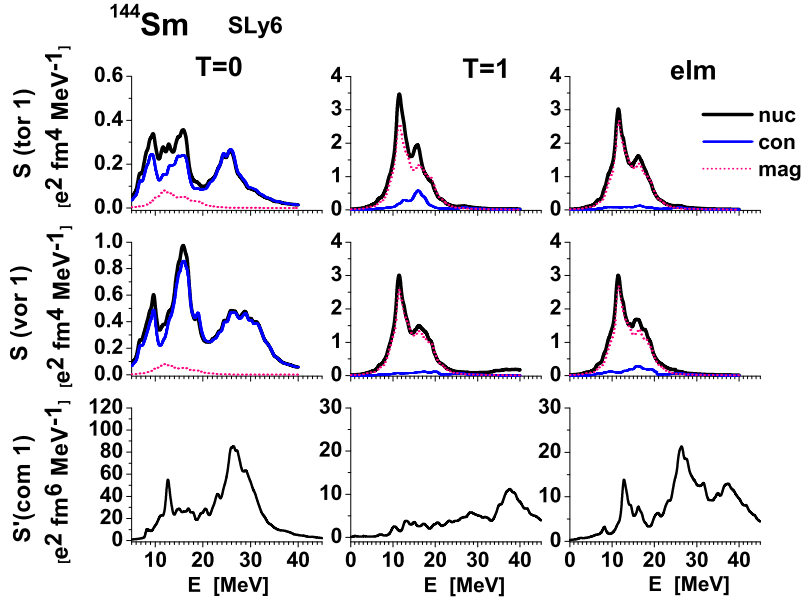

FIG. 8: (color online) RPA toroidal (upper), RW vortical (middle), and compression (bottom) strength functions calculated in T=0 (left), T=1 (middle), and electromagnetic (right) channels with SLy6 Skyrme force in spherical ^{144}Sm. For TM and RW, the contributions from total (black/bold line), convection (blue/thin line), and magnetization (red/dotted line) currents are depicted.

picted in T=0 and T=1 channels. Unlike the CM, the TM is concentrated at low energy while the high-energy strength is rather weak. Following our analysis, this is because of the instructive (destructive) summation of λl=10 and 12 terms in the TM operator (1) in the low-energy (high-energy) regions. For the CM operator (A21) (which may be decomposed in similar manner [18]), we have the opposite result.

The TM(T=0) strength in Fig. 6 demonstrates the same three effects discussed above for CM: i) pumping the strength to the PDR region due to neutron excess/deformation impact, ii) appearance of an apprecia-

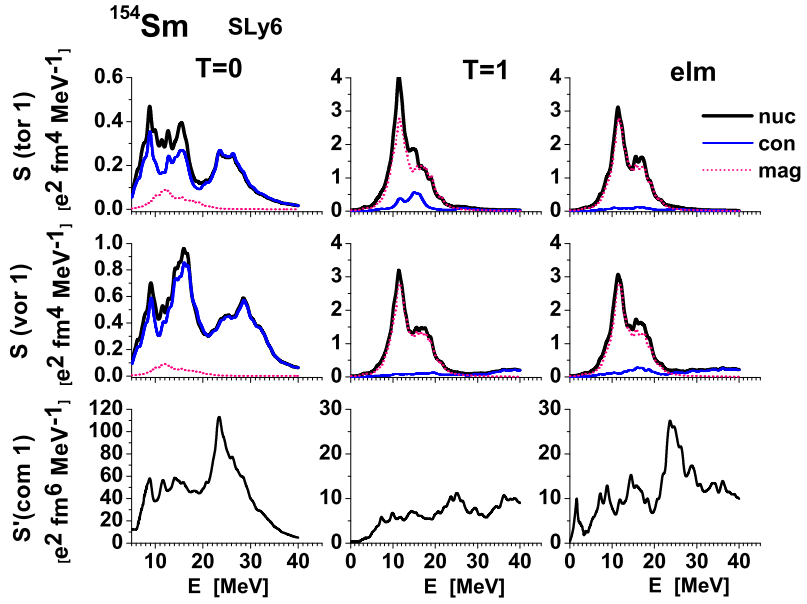

FIG. 9: (color online) The same as in Fig.8 but for deformed ^{154}Sm.

ble μ =0 bump due to the deformation splitting of the high-energy strength, iii) general upshift of the strength with m_0/m. The manifestation of the effects for TM is weaker than for CM and noticeably depends on the force: the effects are significant for SkT6, SVbas, SkM*, SkI3 but small for SLy6. In the T=1 channel, the effects are much weaker, perhaps because the main player, the high-energy TM, is almost absent.

In Fig. 7, a similar behavior is observed for the vortical RW strength generated by the operator (3). The main difference from TM is that low-energy and high-energy RW bumps in T=0 channel are of a comparable strength. Anyway both TM and RW are strong at 5-15 MeV where the maximal nuclear vorticity is expected [18].

Figs. 8 compares in ^{144}Sm the CM, TM, and RW strengths in T=0 and T=1 channels with the strengths in the electromagnetic ('elm') channel relevant for (e, e') reaction, where only the proton part of the transition operators is active, see (9). Fig. 9 does the same for ^{154}Sm. It is seen that the strengths in the 'elm' channel are very similar to T=1 ones. Further Figs. 8 and 9 demonstrate the contributions of the convection $j_{\rm con}$ and magnetization $j_{\rm mag}$ nuclear currents (A9) to the strength. In accordance to the previous calculations for ^{208}Pb [18], the $j_{\rm con}$ dominates at T=0 and $j_{\rm mag}$ at T=1 (and 'elm').

Finally we remark that for a detailed study it is desirable to go beyond RPA and take into account more complex configurations. The low-lying E1 modes, in fact, may couple to two-phonon states describing collective-core excitations coupled to collective surface vibrations, like an octupole-quadrupole excitation. Several RPA extensions are already available. Among them, there are the QRPA plus phonon-coupling model [50, 51] and the separable RPA plus two-phonon approach [54–56] with Skyrme forces, and the relativistic time-blocking approximation (RTBA) [47] embracing the anharmonicity by coupling the RPA phonons to particle-hole + phonon states. Alternatively, one may use the quasiparticle-phonon model (QPM) [52, 53, 57] with Woods-Saxon separable potential and the equation-of-motion phonon method (EMPM) with realistic interactions [58]. All these RPA extensions have been adopted with fair success to describe the low-energy E1 response in nuclei like ^{208}Pb (see e.g. [59–61]) and confirmed an important role played by the multi-phonon states in E1 low-lying spectra. However, before performing more detailed investigations with including multiphonon states, a first exploration with mere RPA exploration is desirable and this is just what we have presented here.

IV. CONCLUSION

The E1 compression, toroidal, and vortical [17] strengths in even Sm isotopes (from spherical ^{144}Sm to deformed ^{154}Sm) were investigated within the self-consistent separable random-phase approximation (SRPA) approach [19, 20] with Skyrme forces. A representative set of different Skyrme parametrizations (SkT6 [27], SVbas [28], SkM* [29], SLy6 [21], and SkI3 [30]) was used. Three reaction channels were inspected: isoscalar (T=0), isovector (T=1) and electromagnetic (with the proton part of the transition operator). Particular attention was paid to effects of the quadrupole deformation.

As a first step, the accuracy of the scheme was checked with respect to binding energies, photoabsorp-

tion cross sections, and E1 energy-weighted sum rules EWSR (isovector for the GDR and isoscalar for the ISGDR). It was shown that the configuration space used in our calculations is large enough to guarantee a good reproduction of the sum rules.

We have analyzed in detail the E1 compressional, toroidal, and vortical strength functions for the chosen variety of the Skyrme forces. The strengths in the electromagnetic channel (relevant for the reaction of inelastic electron scattering) are very similar to T=1 strength. In accordance to our previous explorations for ^{208}Pb [18] and Sn isotopes [22], we find that the convection nuclear current $j_{\rm con}$ plays a dominate role in all T=0 strengths while the magnetization nuclear current $j_{\rm mag}$ is crucial in T=1 and electromagnetic channels.

All strength distributions are upshifted to higher energies with decreasing effective mass m_0 which may be related to the corresponding spreading the single-particle spectra [49]. Following our analysis, Skyrme forces with a high affective masses, $m_0/m = 0.8$–1, are more suitable for the description of the experimental data for the ISGDR [3, 5], whose branches are commonly related to the toroidal and compression modes (TM and CM).

The most interesting results are obtained for the deformation impact on the strengths. There is a dramatic general redistribution of the compressional strength with deformation when passing from spherical ^{144}Sm to deformed ^{154}Sm. In the quasiparticle (HFB) approximation, the deformation splitting of the high-energy CM amounts to as much as 10 MeV. The residual interaction activated in RPA somewhat decreases the effect and reduces the splitting to 5 MeV. However even such a splitting is huge. As a result, the high-energy CM demonstrates a clear separation into μ=0 and μ=1 branches. The μ=0 branch is considerably downshifted and looks more like an individual resonance. This effect is strong for CM and weaker for other strengths. Besides, it is stronger in the T=0 channel than in the T=1 channel. It would be interesting to check our findings in (α, α') experiment for ^{154}Sm.

Besides that, the move from ^{144}Sm to ^{154}Sm causes a considerable redistribution of the strength in the low-energy (PDR) region. This may be attributed to both increasing the number of neutrons and deformation. Following our calculations, the PDR region covers both CM and TM strengths in both T=0 and T=1 channels, see also discussion [22, 23]. Moreover, in accordance to recent experimental analysis [25, 26], the PDR region may be separated into T=0 and T=1 sectors. However, a proper exploration of this detail requires a more involved theoretical framework taking into account the coupling with complex configurations.

Acknowledgments

The work was partly supported by the GSI-F+E-2010-12, Heisenberg-Landau (Germany - BLTP JINR), and Votruba - Blokhintsev (Czech Republic - BLTP JINR) grants. W.K. and P.-G.R. are grateful for the BMBF support under contracts 05P12ODDUE and support from the F+E program of the Gesellschaft für Schwerionenforschung (GSI). The support of the research plan MSM 0021620859 (Ministry of Education of the Czech Republic) and the Czech Science Foundation project No P203-13-07117S to this work are also appreciated.

Appendix A: Vorticity conceptions and the relevant transition operators

1. Velocity and nuclear current fields

In hydrodynamics (HD) [16], the vortical motion of a fluid is characterized by a non-vanishing value of the curl of the velocity field

$$\vec{\nabla} \times \vec{v}_{\rm HD}(\vec{r}) \neq 0 \tag{A1}$$

where $\vec{v}(\vec{r})$ is defined as a time derivative of the displacement field, see e.g. [12]. Instead, a quantum-mechanical treatment of the nuclear vorticity should involve the actual nuclear physical observables, namely the nuclear current defined by the operator

$$\hat{\vec{j}}_{\rm nuc}(\vec{r}) = \sum_{\nu\nu'} \langle\nu|\, \hat{\vec{j}}(\vec{r})\, |\nu'\rangle\, a^+_\nu a_{\nu'}, \tag{A2}$$

where a^+_ν, a_ν are single particle (s.p.) creation and annihilation operators, respectively. The nuclear current consists of a convection and a magnetization parts:

$$\hat{\vec{j}}_{\rm nuc} = \hat{\vec{j}}_{\rm con} + \hat{\vec{j}}_{\rm mag}. \tag{A3}$$

Thus the current transition density (CTD) reads

$$\langle\nu|\, \hat{\vec{j}}_{\rm nuc}(\vec{r})\, |\nu'\rangle = \langle\nu|\, \hat{\vec{j}}_{\rm con}(\vec{r})\, |\nu'\rangle + \langle\nu|\, \hat{\vec{j}}_{\rm mag}(\vec{r})\, |\nu'\rangle. \tag{A4}$$

The convection CTD is given by

$$\langle\nu|\, \hat{\vec{j}}(\vec{r})_{\rm con}\, |\nu'\rangle = \frac{i\, e^{\rm eff}_q \hbar}{2m} \times \left[(\vec{\nabla}\Psi_\nu(\vec{r}))^+ \Psi_{\nu'}(\vec{r}) - \Psi^+_\nu(\vec{r}) \vec{\nabla}\Psi_{\nu'}(\vec{r}) \right], \tag{A5}$$

where $\Psi^+_\nu(\vec{r})$ are s.p. wave functions and $e^{\rm eff}_q$ is a proton (q=p) or neutron (q=n) effective charge. The magnetization CTD has the form

$$\langle\nu|\, \hat{\vec{j}}_{\rm mag}(\vec{r})\, |\nu'\rangle = \frac{e\hbar}{2m}\, g^{\rm eff}_q\, \Psi^+_\nu(\vec{r})\, (\vec{\nabla} \times \vec{\sigma})\, \Psi_{\nu'}(\vec{r}), \tag{A6}$$

where $g^{\rm eff}_q$ is the effective gyromagnetic ratio.

As shown below, the nuclear vorticity may be defined either following a semi-classical HD approach, see e.g. [12, 16], or a quantum-mechanical RW route [17].

2. HD treatment of the vorticity

In this approach, the spin part of the nuclear current is usually neglected. Then one may define the velocity operator $\hat{\vec{v}}_{\rm HD}$ through the nuclear current operator as

$$\hat{\vec{j}}_{\rm nuc}(\vec{r}) = \rho_0(\vec{r})\, \hat{\vec{v}}_{\rm HD}(\vec{r}), \tag{A7}$$

where $\rho_0(\vec{r})$ is the density in the ground state. After taking the curl of the current (A7), we obtain the quantity

$$\rho_0(\vec{r})\, \vec{\nabla} \times \hat{\vec{v}}_{\rm HD}(\vec{r}) = \vec{\nabla} \times \hat{\vec{j}}_{\rm nuc}(\vec{r}) - \vec{\nabla}\rho_0(\vec{r}) \times \hat{\vec{v}}_{\rm HD}(\vec{r}) =$$
$$= \vec{\nabla} \times \hat{\vec{j}}_{\rm nuc}(\vec{r}) - \vec{\nabla}\rho_0(\vec{r}) \times \frac{\hat{\vec{j}}_{\rm nuc}(\vec{r})}{\rho_0(\vec{r})} \tag{A8}$$

which may be adopted to measure the nuclear vorticity. This definition, however, does not take into account that the charge and current densities are not independent but related by the continuity equation.

3. RW treatment of the vorticity

In order to eliminate the drawback of the hydrodynamical definition, the RW prescription [17] starts with decomposing the nuclear current into an irrotational and a vortical components

$$\hat{\vec{j}}_{\rm nuc}(\vec{r}) = \hat{\vec{j}}_{\rm irrot}(\vec{r}) + \hat{\vec{j}}_{\rm vort}(\vec{r}) \tag{A9}$$

It is further assumed that the quantity

$$\hat{\vec{w}}(\vec{r}) \;\equiv\; \vec{\nabla} \times \hat{\vec{j}}_{\rm vort}(\vec{r}) =$$
$$=\; \vec{\nabla} \times \hat{\vec{j}}_{\rm nuc}(\vec{r}) - \vec{\nabla} \times \hat{\vec{j}}_{\rm irrot}(\vec{r}) \tag{A10}$$

is a measure of a vortical flow. This motion sets in once $\langle f|\, \hat{\vec{w}}(\vec{r})\, |i\rangle \neq 0$ and vice versa.

One proceeds with a multipole decomposition in terms of spherical harmonics $Y_{\lambda\mu}(\hat{r})$ or vector spherical $\vec{Y}_{\lambda l\mu}(\hat{r})$ harmonics obtaining

$$\langle f|\, \hat{\vec{w}}_{\rm nuc}(\vec{r})\, |i\rangle = \sum_{l\lambda\mu} b^{(fi)}_{\lambda\mu}\, w_{\lambda l}(r)\, \vec{Y}_{\lambda l\mu}(\hat{r}), \tag{A11}$$

where

$$b^{(fi)}_{\lambda\mu} = \frac{(j_i m_i \lambda\mu | j_f m_f)}{\sqrt{2j_f+1}} \tag{A12}$$

and

$$w^{(fi)}_{\lambda\lambda}(r) = \sqrt{\frac{2\lambda+1}{\lambda}}\, \left(\frac{d}{dr} + \frac{\lambda+2}{r}\right)\, j^{(fi)}_{\lambda\,\lambda+1}(r), \tag{A13}$$

which follows from applying the continuity equation.

Using the the multipole decomposition, the second term in (A10) can be written as

$$\left[\vec{\nabla} \times \hat{\vec{j}}_{\rm irrot}(\vec{r})\right]_\lambda = \frac{1}{\lambda}\, \left[(\vec{\nabla}\hat{\rho}(\vec{r})) \times \hat{\vec{r}}\right]_\lambda . \tag{A14}$$

This quantity resembles the second term in the hydrodynamic equation (A8). It is therefore legitimate to adopt the matrix element (A11) as a measure of vorticity [17].

4. RW vortical operator

The vortical multipole operator was introduced in [18]. One starts with the standard $E\lambda$ multipole operator [**?**]

$$\hat{M}(E\lambda\mu, k) = \frac{(2\lambda+1)!!}{ck^{\lambda+1}} \sqrt{\frac{\lambda}{\lambda+1}} \tag{A15}$$
$$\cdot \int d^3r\, [\, j_\lambda(kr)\, \vec{Y}_{\lambda\lambda\mu}(\hat{\vec{r}})\,] \cdot [\vec{\nabla} \times \hat{\vec{j}}_{nuc}(\vec{r})].$$

After expanding the spherical Bessel functions $j_\lambda(kr)$ in powers of (kr) and using the continuity equation, one obtains [11]

$$\hat{M}(E\,\lambda\mu;\, k) = \hat{M}(E\lambda\mu) + k\, \hat{M}(\mathrm{tor};\, \lambda\mu) + \ldots, \tag{A16}$$

where $\hat{M}(E\lambda\mu)$ and $\hat{M}(\mathrm{tor};\, \lambda\mu)$ are, respectively, the long-wavelength limits of the standard and toroidal $E\lambda$ multipole operators [11, 18]

$$\hat{M}(E\,\lambda\mu) = -\int\, d^3r\, \hat{\rho}(\vec{r})\, r^\lambda\, Y_{\lambda\mu}(\hat{r}), \tag{A17}$$

$$\hat{M}(\mathrm{tor};\, \lambda\mu) = -\frac{\mathrm{i}}{2\mathrm{c}} \sqrt{\frac{\lambda}{2\lambda+1}} \int\, \mathrm{d}^3\mathrm{r}\hat{\vec{\mathrm{j}}}_{\rm nuc}(\vec{\mathrm{r}}) \tag{A18}$$
$$\cdot r^{\lambda+1} \left[\, \vec{Y}_{\lambda\,\lambda-1\,\mu}(\vec{r}) + \sqrt{\frac{\lambda}{\lambda+1}}\, \frac{2}{2\lambda+3}\, \vec{Y}_{\lambda\,\lambda+1\,\mu}(\vec{r}) \right].$$

The minus sign in $\hat{M}(E\,\lambda\mu)$ is appropriate for excitations processes ($E_f > E_i$).

According to the RW concept of vorticity [17], the vortical multipole operator $\hat{M}(\mathrm{vor};\, \lambda\mu;\, \mathrm{k})$ is obtained from (A15) by the substitution

$$\left[\, \vec{\nabla} \times \hat{\vec{j}}_{\rm nuc}(\vec{r})\, \right] \;\rightarrow\; \hat{\vec{w}}(\vec{r}) = \vec{\nabla} \times \hat{\vec{j}}_{\rm nuc}(\vec{r}) - \vec{\nabla} \times \hat{\vec{j}}_{\rm irrot}(\vec{r}). \tag{A19}$$

Using (A14), one gets in the long wavelength limit

$$\hat{M}(\mathrm{vor};\, \lambda\mu;\, \mathrm{k}) = \mathrm{k}\, \hat{\mathrm{M}}(\mathrm{vor};\, \lambda\mu) + \ldots$$
$$= k\, \left[\, \hat{M}(\mathrm{tor};\, \lambda\mu) + \hat{\mathrm{M}}(\mathrm{com};\, \lambda\mu)\, \right] + \ldots \tag{A20}$$

The toroidal term $\hat{M}(\mathrm{tor};\, \lambda\mu)$ is given by (A17) and the compressional operator is

$$\hat{M}(\mathrm{com};\, \lambda\mu) = -\mathrm{k}\, \hat{\mathrm{M}}'(\mathrm{com};\, \lambda\mu), \tag{A21}$$

where $\hat{M}'(\mathrm{com};\, \lambda\mu)$ is the familiar compression multipole operator [11, 15]

$$\hat{M}'(\mathrm{com};\, \lambda\mu) = \frac{1}{2\,(2\lambda+3)} \int\, \mathrm{d}^3\mathrm{r}\hat{\rho}(\vec{\mathrm{r}})\mathrm{r}^{\lambda+2}\mathrm{Y}_{\lambda\mu}(\hat{\mathrm{r}}). \tag{A22}$$

From the above equations it follows [18] that the vorticity multipole operator has the form

$$\hat{M}(\mathrm{vor};\, \lambda\mu) = \hat{\mathrm{M}}(\mathrm{tor};\, \lambda\mu) + \hat{\mathrm{M}}(\mathrm{com};\, \lambda\mu)$$
$$= -\frac{i}{c}\, \frac{1}{2\lambda+3} \sqrt{\frac{2\lambda+1}{\lambda+1}} \int\, d^3r\, \hat{\vec{j}}_{\rm nuc}(\vec{r})$$
$$\cdot\, r^{\lambda+1}\, \vec{Y}_{\lambda\,\lambda+1\,\mu}(\hat{r}). \tag{A23}$$

This definition shows that the vortical operator $\hat{M}$(vor; $\lambda\mu$; k) (A20) is a first order correction to the leading $E\lambda$ operator (A15).

For the dipole transitions, the operators are to be accordingly modified in order to remove the spurious contribution induced by the center of mass motion. Following [18], only the toroidal (1) and compressional (2) operators are actually modified, while the vorticity operator (3) remains unchanged.

Appendix B: SRPA approach

The SRPA Hamiltonian is self-consistently derived [19, 20] from the functional [62]

$$\mathcal{E} = \mathcal{E}_{\rm kin} + \mathcal{E}_{\rm Sk} + \mathcal{E}_{\rm pair} + \mathcal{E}_{\rm Coul} \tag{B1}$$

involving kinetic-energy, Skyrme, pairing, and Coulomb terms. The Skyrme functional $\mathcal{E}_{\rm Sk}(\rho, \tau, \vec{J}, \vec{j}, \vec{s}, \vec{T})$ [63–65] depends on the time-even nucleon (ρ), kinetic-energy (τ), and spin-orbit ($\vec{J}$) densities as well as on the time-odd current ($\vec{j}$), spin ($\vec{s}$), and vector kinetic-energy ($\vec{T}$) densities.

The Hamiltonian is composed of the HFB mean field and residual potential [19, 20]

$$\hat{H} = \hat{h}_{\rm HFB} + \hat{V}_{\rm res}. \tag{B2}$$

The HFB mean field is given by

$$\hat{h}_{\rm HFB} = \int d^3r \sum_{\alpha_+} [\frac{\delta\mathcal{E}}{\delta J_{\alpha_+}(\vec{r})}] \hat{J}_{\alpha_+}, \tag{B3}$$

where J_{α_+} (J_{α_-}) are time even (odd) densities and $\hat{J}_{\alpha_\pm}$ are the corresponding operators, with α_+ (α_-) denoting the densities.

The residual interaction is a sum of separable pieces

$$\hat{V}_{res} = \frac{1}{2} \sum_{k,k'=1}^{K} (\kappa_{kk'} \hat{X}_k \hat{X}_{k'} + \eta_{kk'} \hat{Y}_k \hat{Y}_{k'}) \tag{B4}$$

with one-body fields

$$\hat{X}_k = i \int d^3r d^3r' \sum_{\alpha_+,\alpha'_+} \frac{\delta^2\mathcal{E}}{\delta J_{\alpha_+} \delta J_{\alpha'_+}} \langle [\hat{P}_k, \hat{J}_{\alpha_+}] \rangle \hat{J}_{\alpha'_+} \tag{B5}$$

$$\hat{Y}_k = i \int\int d^3r d^3r' \sum_{\alpha_-,\alpha'_-} \frac{\delta^2\mathcal{E}}{\delta J_{\alpha_-} \delta J_{\alpha'_-}} \langle [\hat{Q}_k, \hat{J}_{\alpha_-}] \rangle \hat{J}_{\alpha'_-}$$

and strength constants

$$\kappa^{-1}_{kk'} = -i\langle [\hat{P}_k, \hat{X}_{k'}] \rangle \ , \quad \eta^{-1}_{kk'} = -i\langle [\hat{Q}_k, \hat{Y}_{k'}] \rangle \ . \tag{B6}$$

The fields $\hat{X}_k$ and $\hat{Y}_k$ are time-even and time-odd, respectively. The corresponding generators are time-odd $\hat{P}_k = i[\hat{H}, \hat{Q}_k]$ and time-even $\hat{Q}_k$.

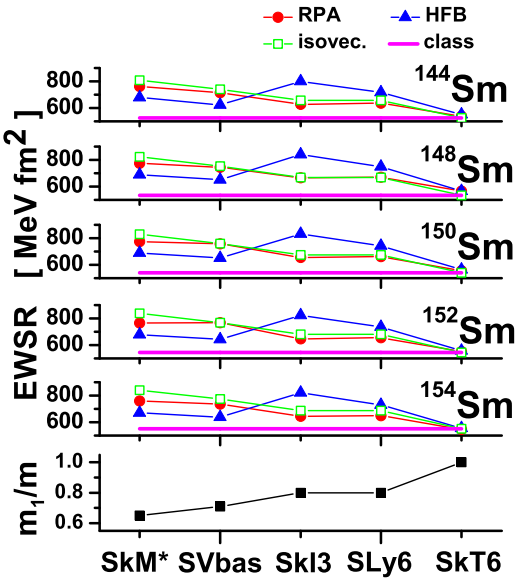

FIG. 10: (color online) The HF/HFB (blue curve with triangles) and RPA (red curve with circles) EWSR in $^{144-154}$Sm isotopes, calculated with different Skyrme forces. For the comparison, the TRK values computed with the bare nucleon mass m (pink horizontal line) and isovector effective mass m_1 (green curve with rectangles) are depicted. The values of m_1/m are given in the low panel.

The two-body potential includes all possible separable terms allowed by the functional. In practice, the number of fields is determined by the number of the generators $\hat{Q}_k$ or $\hat{P}_k$ chosen as input. Such a choice is crucial for generating a minimal set of one-body fields appropriate for the excitation mode to be studied and, therefore, render feasible the numerical implementation. An optimal set of generators were determined for $E1$ [19, 20] and $M1$ [35, 36] modes. The set of generators needed for the modes under investigation here was discussed in the Appendix D of Ref. [18]. The Skyrme separable RPA may be also derived by an alternative way [54, 55].

The self-consistent separable form (B4) of the residual interaction enables us to transform the RPA equations of motion into a system of homogeneous algebraic equations in the forward $c_{ij}^{(\nu q-)}$ and backward $c_{ij}^{(\nu q+)}$ amplitudes of the RPA phonon creation operators [19]

$$\hat{C}^+_\nu = \sum_{q=n,p} \sum_{ij\in q} \left(c_{ij}^{(\nu q-)} \alpha_i^+ \alpha_j^+ - c_{ij}^{(\nu q+)} \alpha_j \alpha_i \right), \tag{B7}$$

where α_i^+ and α_i are quasiparticle creation and annihilation operators, respectively. The rank of the matrix of the system of algebraic equations is 4K, where K is the number of separable terms in (B4). Usually $K = 3-5$ is sufficient to describe a given mode [19, 35]. So low rank

allows very efficient and fast solution of the SRPA equations. They yield one-phonon states $\mid \nu\rangle = \hat{C}^+_\nu \mid \mathrm{RPA}\rangle$ of energy E_ν, with $\mid \mathrm{RPA}\rangle$ being the phonon vacuum.

Appendix C: Thomas-Reiche-Kuhn sum rule

In Fig. 10, the integral HFB and RPA energy-weighted strengths (10) are compared to the TRK sum rule for the Skyrme forces [40, 67]

$$\mathrm{EWSR}_{\mathrm{TRK}} = \frac{9\,\hbar^2}{8\pi m_1}\,\frac{NZ}{A}\,. \qquad \text{(C1)}$$

Unlike the common case [40], this expression includes not the bare nucleon mass m but the isovector effective mass m_1 so as to take into account the contribution of the velocity-dependent terms (VDT) of the Skyrme forces, see an extensive discussion in Refs. [33, 67]. It is seen that, for all Skyrme forces, the RPA strengths follow closely the TRK values. The agreement takes place both for m_1/m <1 (SkM*, SVbas, SkI3, SLy6 with active VDT) and m_1/m =1 (SkT6 with zero VDT). This implies that i) m_1 successfully incorporates almost all VDT contributions to the EWSR, ii) our configuration space is sufficiently large. For most of the forces, the HFB and RPA values overestimate by 20-30% the TRK values evaluated with the bare nucleon mass m. This indicates an important role of the VDT. Besides, the VDT causes a substantial difference between HFB and RPA results.

Note that unlike the TRK sum rule (C1), the isoscalar EWSR for the ISGDR [43] (14) uses the bare mass m. Following [67], the VDT contribute to both mean field and residual interaction but, for T=0 RPA calculations, these contributions almost compensate each other. Thus we may use the bare mass m. Instead, for T=1 RPA calculations considered above, the compensation does not take place, which results in using m_1 in (C1).

[1] H. L. Clark, Y. W. Lui, and D. H. Youngblood, Phys. Rev. C **63**, 031301(R) (2001).
[2] D. H. Youngblood, Y. W. Lui, H. L. Clark, B. John, Y. Tokimoto, and X. Chen, Phys. Rev. C **69** 034315 (2004).
[3] M. Itoh *et al*, Phys. Rev. C 68, 064602 (2003).
[4] M. Uchida *et al*, Phys. Lett. B **557**, 12 (2003).
[5] M. Uchida *et al.*, Phys. Rev. C **69**, 051301(R) (2004).
[6] N. Paar, D. Vretenar, E. Khan, and G. Colo, Rep. Prog. Phys. **70**, 691 (2007).
[7] D. Vretenar, A. Wandelt, and P. Ring, Phys. Lett. B **487**, 334(2000).
[8] G. Colò, N. Van Giai, P. F. Bortignon, and M. R. Quaglia, Phys. Lett. B **485**, 362 (2000).
[9] S. I. Bastrukov, S. Misicu, and V. I. Sushkov, Nucl. Phys. A **562**, 191(1993).
[10] D. Vretenar, N. Paar, P. Ring, and T. Niksic, Phys. Rev. C **65**, 021301(R)(2002).
[11] J. Kvasil, N. Lo Iudice, Ch. Stoyanov, and P. Alexa, J. Phys. G: Nucl. Part. Phys. **29**, 753 (2003).
[12] S. Misicu, Phys. Rev. C **73**, 024301 (2006).
[13] V.M. Dubovik and A.A. Cheshkov, Sov. J. Part. Nucl. **5**, 318 (1975).
[14] V. M. Dubovik and L. A. Tosunyan, Sov. J. Part. Nucl. **14**, 504 (1983).
[15] S.F. Semenko, Sov. J. Nucl. Phys. **34**, 356 (1981).
[16] L. D. Landau and E. M. Lifshitz, *Course of Theoretical Physics: Hydrodynamics* Vol. 6, (Butterworth-Heinemann, Oxford, 1987).
[17] D.G. Raventhall, J. Wambach, Nucl. Phys. A**475**, 468 (1987).
[18] J. Kvasil, V.O. Nesterenko, W. Kleinig, P.-G.Reinhard, and P.Vesely, Phys.Rev. C **84**, 034303 (2011).
[19] V.O. Nesterenko, J. Kvasil, and P.-G. Reinhard, Phys. Rev. C **66**, 044307 (2002).
[20] V.O. Nesterenko, W. Kleinig, J. Kvasil, P. vesely, P.-G. Reinhard, and D.S. Dolci, Phys.Rev. C **74**, 064306 (2006).
[21] E. Chabanat, P. Bonche, P. Haensel, J. Meyer, and R. Schaeffer, Nucl. Phys. A **627**, 710 (1997).
[22] J. Kvasil, V.O. Nesterenko, A. Repko, W. Kleinig, P.-G. Reinhard, and N. Lo Iudice, Phys, Scr. **T154**, 014019 (2013).
[23] A. Repko, P.-G. Reinhard, V.O. Nesterenko, and J. Kvasil, Phys. Rev. C**87**, 024305 (2013).
[24] P.-G. Reinhard, Ann. Physik, **1**, 632 (1992).
[25] J. Endres *et al.*, Phys. Rev. C **85**, 064331 (2012))
[26] D. Savran *et al.*, Phys. Rev. C **84**, 024326 (2011) .
[27] F. Tondeur, M. Brack, M. Farine, and J.M. Pearson, Nucl. Phys. A **420**, 297 (1984).
[28] P. Kluepfel, P.-G. Reinhard, T.J. Buervenich, and J.A. Maruhn, Phys. Rev. C **79**, 034310 (2009).
[29] J. Bartel, P. Quentin, M. Brack, C. Guet, and H.-B. Haakansson, Nucl. Phys A **386**, 79 (1982).
[30] P.-G. Reinhard and F. Flocard, Nucl. Phys. A **584**, 467 (1995).
[31] V.O. Nesterenko, W. Kleinig, J. Kvasil, P. Vesely, P.-G. Reinhard, Int. J. Mod. Phys. E**16**, 624 (2007).
[32] W. Kleinig, V.O. Nesterenko, J. Kvasil, P. Vesely, P.-G. Reinhard, Phys.Rev. C**78**, 044313 (2008).
[33] V.O. Nesterenko, W. Kleinig, J. Kvasil, P. Vesely, and P.-G. Reinhard, Int. J. Mod. Phys. E**17**, 89 (2008).
[34] J. Kvasil, V.O. Nesterenko, W. Kleinig, D. Bozik, and P.-G. Reinhard, Int. J. Mod. Phys. E **20**, 281 (2011).
[35] P. Vesely, J. Kvasil, V.O. Nesterenko, E. Kleinig, P.-G. Reinhard, and V.Yu. Ponomarev, Phys. Rev. C **80**, 031302(R) (2009).
[36] V.O. Nesterenko, J. Kvasil, P. Vesely, W. Kleinig, P.-G. Reinhard, and V.Yu. Ponomarev, J.Phys.G: Nucl. Part. Phys. **37**, 064034 (2010).
[37] V.O. Nesterenko, J. Kvasil, P. Vesely, W. Kleinig, and P.-G. Reinhard, Int. J. Mod. Phys. (E) **19**, 558 (2010).
[38] J. Kvasil, P. Vesely, V.O. Nesterenko W. Kleinig, P.-G. Reinhard, and S. Frauendorf, Int. J. Mod. Phys. E**18**, 975 (2009).
[39] R. Alarcon, R.M. Laszewski, and D.S. Dale, Phys. Rev. C **40**, R1097 (1989).
[40] P. Ring, P. Schuck, Nuclear Many Body Problem, (Springer-Verlag, New York, 1980).

[41] A.V. Varlamov, V.V. Varlamov, D.S. Rudenko, and M.E. Stepanov, *Atlas of Giant Dipole Resonances*, INDC(NDS)-394, 1999; JANIS database.

[42] http://www.oecd-nea.org/janis

[43] M.N. Harakeh and A. van der Woude, *Giant Resonances* (Clarendon Press, Oxford, 2001).

[44] G. Colò, C. Ligang, Nguyen Van Giai, and L. Capelli, Computer Phys. Communication **184**, 142 (2013).

[45] M. Bender, K. Rutz, P.-G. Reinhard, and J.A. Maruhn, Eur. Phys. J. A **8**, 59 (2000).

[46] J. Endres et al., Phys. Rev. Lett. **105**, 212503 (2010).

[47] E. Litvinova, P. Ring, and V. Tselyaev, Phys. Rev. C**78**, 014312 (2008).

[48] http://www.nndc.bnl.gov/amdc/

[49] V.O. Nesterenko, V.P. Likhachev, P.-G. Reinhard, V.V. Pashkevich, W. Kleinig, and J. Mesa, Phys. Rev. C**70**, 057304 (2004).

[50] G. Colò, N. Van Giai, P. F. Bortignon, and R. A. Broglia, Phys. Rev. C **50**, 1496 (1994).

[51] G. Colò and P. F. Bortignon, Nucl. Phys. A **696**, 427 (2001).

[52] V. G. Soloviev, *Theory of atomic nuclei : Quasiparticles and Phonons* (Institute of Physics, Bristol, 1992).

[53] V.Yu. Ponomarev, P.F. Bortignon, R.A. Broglia, E. Vigezzi, and V.V. Voronov, Nucl. Phys. A **599**, 341c (1996)

[54] Nguyen Van Giai, Ch. Stoyanov, V.V. Voronov, Phys. Rev. C**57**, 1204 (1998).

[55] A.P. Severyukhin, V.V. Voronov, Nguyen Van Giai, Phys. Rev. C**77**, 024322 (2008).

[56] N. N. Arsenyev, A. P. Severyukhin, V. V. Voronov, and Nguen Van Giai, arXiv:1209.6146 [nucl-th].

[57] N. Lo Iudice, V. Yu. Ponomarev, Ch. Stoyanov, A. Sushkov, and V. V. Voronov, J. of Phys. G: Nucl. Part. Phys. **39**, 043101 (2012).

[58] D. Bianco,F. Knapp, N. Lo Iudice, F. Andreozzi, and A. Porrino Phys. Rev. C **84**, 014313(2012).

[59] D. Bianco,F. Knapp, N. Lo Iudice, F. Andreozzi, and A. Porrino Phys. Rev. C **86**,(2012).

[60] A. Tamii *et al.*, Phys. Rev. Lett. **107**, 062502 (2011)

[61] I. Poltoratska *et al.*, Phys. Rev. C **85**, 041304(R) (2012).

[62] M. Bender, P.-H. Heenen, and P.-G. Reinhard, Rev. Mod. Phys. **75**, 121 (2003).

[63] T.H.R. Skyrme, Phil. Mag. **1**, 1043 (1956).

[64] D. Vauterin, D.M. Brink, Phys. Rev. **C5**, 626 (1972).

[65] Y.M. Engel, D.M. Brink, K. Goeke, S.J. Krieger, and D. Vauterin, Nucl. Phys. A**249**, 215 (1975).

[66] S. Raman, C.H. Malarkey, W.T. Milner, C.W. Nesdov, J.R. and P.H. Stelson, At. Data Nucl. Data Tables **36**, 1 (1987).

[67] E. Lipparini and S. Stringari, Phys. Rep. **175**, 103 (1989).